Spectral Analysis of Supersonic Cylinder Wake

Mentor

Professor Joseph E. Shepherd

Report by

Taehan Lee

In Partial Fulfillment of the Requirements for the

Caltech Summer Undergraduate Research Fellowship

Caltech

CALIFORNIA INSTITUTE OF TECHNOLOGY

Pasadena, California

ACKNOWLEDGEMENTS

The work represented in this report would not have been possible without the support and attention of a group of individuals. First and foremost, I would like to thank Professor Joseph E. Shepherd for providing me with this incredible opportunity and offering me mentorship and advice of the highest caliber. His cultivation of a curious and hard-working group culture was instrumental in making my time at Caltech both productive and rewarding. Learning under his stewardship this summer has directly contributed to my passion for research.

I also want to thank Professor Joanna M. Austin who provided invaluable feedback and advice throughout the course of my project. Her deep understanding of experimental high-speed gasdynamics was a rich resource from which I drew many times throughout this summer. I am especially grateful for her trust in giving me the independence to carry a project from its initial conception through its execution and analysis, allowing me to experience and contribute to every stage of the research process. Additionally, I want to thank Professor Hans G. Hornung, whose guidance and mentorship throughout my project meant the world to me.

William Feasey was an instrumental component of the success of this project. He patiently worked alongside me day by day, helping me resolve the wide range of challenges that arose. He displayed an incredible work ethic and inspired me to pursue my project with the same curiosity and vigor. His ability to think through complex problems and generate miniature experiments to test our ideas grew me as a researcher and student. Furthermore, I would like to thank Noel Esparza-Duran who fostered my curiosity in the laboratory. He helped me not only design and implement my work in the Ludwieg Tube but also allowed me to learn the intricacies of the T5 Shock Tunnel and barrage him with questions about these amazing facilities. In the rush of the typical summer project, Ali Kiani worked extremely hard to ensure that my components were manufactured on schedule. Without his diligent work, none of the results in this project would have been obtained.

I would also like to acknowledge the fellow undergraduates that populated our group: Lucas J. Favretto, Jorge S. Sanchez, Luis Y. Serrano Laguna, and Reema Almadhi. They collectively created a team culture of hard work, respect, and passion. To have the pleasure of discussing my work with them and learning about their projects was an integral part of the summer research experience.

ABSTRACT

Supersonic cylinder wake is a fundamental case of compressive bluff-body flow. To image and analyze the wake flowfield, this project utilized high-speed schlieren imaging in combination with Spectral Proper Orthogonal Decomposition (SPOD) to characterize the acoustic mechanisms within the wake. The data was collected in the Caltech Ludwieg Tube, a blowdown Mach 4 facility particularly suitable for well-converged spectral analysis techniques due to its extended test-time capabilities. A longer cylinder model was designed to improve upon previous work. By varying the upstream pressure and cylinder diameter, a series of Reynolds numbers ranging from $8.9E4$ to $4.89E5$ were studied. Flowfield-wise SPOD analysis reveals a clear harmonic mechanism associated with a constant Strouhal number $St_s \approx 0.48$. These modes reveal a clear mechanism by which instabilities propagate downstream through the sliplines and feed into the neck. SPOD analysis conducted within the dead-air region resolves upstream acoustic structures supporting the existence of an aeroacoustic feedback loop that maintains the coherent oscillations previously observed in supersonic cylinder wake flow. With the successful imaging of upstream propagating acoustic waves in the dead-air region, an opportunity for future work exists to further characterize the properties of these waves and their interactions with the separation point and sliplines.

TABLE OF CONTENTS

Acknowledgements ii

Abstract iii

Table of Contents iv

Background & Motivation 1

Results 5

1. Flowfield-Wide Results 5
2. Dead-Air Results 9

Methods 12

3. Caltech Ludwieg Tube 12
4. Model Design & Structural Validation 15
5. Schlieren Imaging 18
6. Proper Orthogonal Decomposition 21
7. Spectral Proper Orthogonal Decomposition 25

Conclusion 30

References 31

Appendix 32

BACKGROUND & MOTIVATION

This project falls within the subfield of aeronautical engineering known as compressive bluff-body flow. In a sense, all designs of aeronautical vehicles and devices rely on the understanding of the physical interaction between fluid flow and structure (such as the device's airframe or control surfaces). In aeronautical engineering a bluff-body refers to a geometry that promotes flow separation and the formation of a wake, thereby generating unsteady aerodynamic forces on the structure. Bluff bodies are often used extensively in reentry vehicles traveling faster than the speed of sound, a flow regime known as supersonic. In this regime, compressibility effects and shock waves become increasingly important, making the resulting wake dynamics more complex than in subsonic flow. Understanding the fundamental flow physics governing bluff-body wakes, particularly in the supersonic regime, is therefore essential for predicting and mitigating these instabilities on the vehicle.

In compressible flow, disturbances propagate at the local speed of sound relative to the fluid. If the flow is supersonic, disturbances coalesce into shock waves. If an obstruction, such as a reentry space capsule, is introduced to the flow, these shock waves communicate its influence through the fluid. As a result, flow upstream of a shockwave is unaware or unperturbed by the obstruction, and is only affected by the obstruction through the shockwave itself. Bluff-bodies will generate a detached bow shock, due to their often blunt geometry. Experimental images displaying the visual differences of supersonic bluff-body flow are shown in Figure 1.

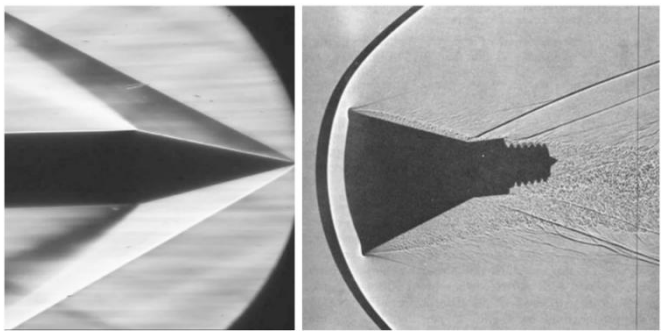


Figure 1.

Left Schlieren image of attached shockwaves on a sharp cone (Venkatakrishnan 2004)
Right Shadowgraph image of a detached bow shock ahead of bluff-body (NASA 1960)

The work represented by this report aims to study the fundamental flow physics of supersonic bluff-body wake flow by carefully studying a canonical case: supersonic cylinder wake. Cylinder flow has always represented a formative example in understanding any flow regime. Supersonic flow, however, presents unique challenges that require careful and modern techniques to overcome. This will be more carefully described in the coming paragraphs.

In the case of subsonic, incompressible flow cylinder wake is well understood to exhibit behavior governed by hydrodynamic interaction. This includes the classic Kármán vortex street, which has formed the foundation of much turbulence and wake flow understanding (King 1977).

Despite a long history of study, a similarly mature understanding does not yet conclusively exist in the case of supersonic, compressible flow around cylinders. The difficulty lies in the fact that supersonic wake flow is comprised of high-frequency, acoustic phenomena. Where subsonic vortex shedding can sometimes occur at frequencies in the order of 10 Hz, supersonic cylinder wake flow often has characteristic frequencies in the order of 10^3 to 10^4 Hz. It follows that for experiments to successfully capture interactions occurring in this range of frequencies, the usage of high-speed cameras and imaging techniques is required. It is this barrier that has kept the study of supersonic cylinder wake relevant in modern times, as reliable high-speed imaging technologies have only become available very recently. Images showing the difference between incompressible vortex shedding and supersonic cylinder wake are shown in Figure 2.

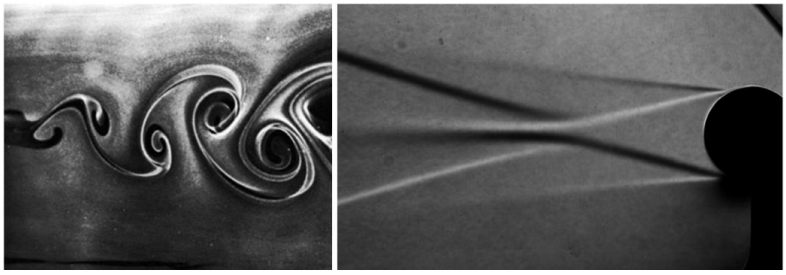


Figure 2.
Left Kármán vortex street schlieren image (White 1994)
Right Supersonic cylinder wake schlieren image from this project

Despite these challenges, significant work was completed very early in the study of this phenomenon. An important example is work completed by Gowen and Perkins in 1953. Reported in this technical document is the measurement of coefficients of drag for cylinders at a range of flow speeds, including the supersonic regime. During the measurements, a shadowgraph image was taken of the flowfield which is shown in Figure 3.

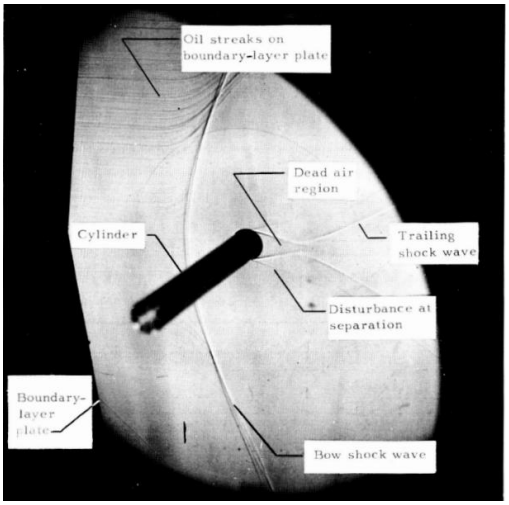


Figure 3. Shadowgraph of flow about a cylinder at Mach 1.49 (Gowen 1953)

Even at this early point in the study of supersonic cylinder wake, much could be understood regarding the basic anatomy of the flowfield. As supersonic flow encounters the cylinder a bow shock forms a certain standoff-distance from the cylinder itself. Although the flow becomes subsonic directly in front of the cylinder, it is still supersonic above and below the cylinder. As such, the flow expands around the cylinder and separates off the back half. This creates two sliplines that bound the dead-air region. Outside of the sliplines there are supersonic flows travelling approximately parallel to the sliplines. Inside the dead-air region is subsonic recirculating flow. As these two supersonic flows meet along the centerline, they create a neck and generate oblique trailing shock waves to turn the flow back to parallel. A diagram of this flowfield is shown in Figure 4.

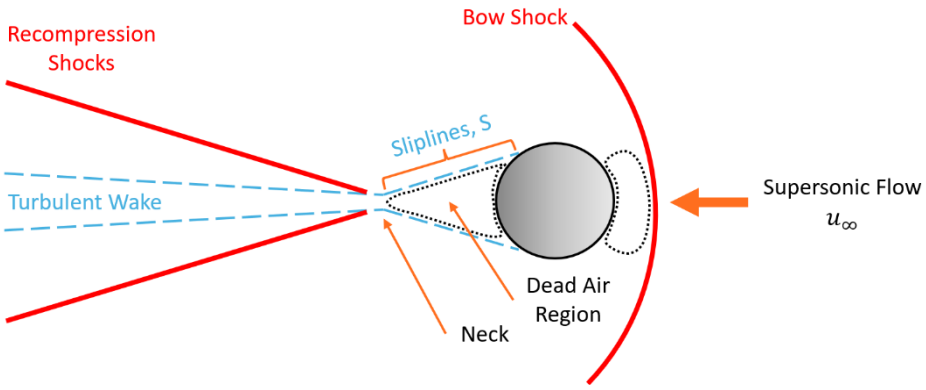


Figure 4. Diagram of supersonic cylinder flowfield

Modern efforts in this topic have centered on understanding the characteristic physical mechanism that comprises this wake flow. Schmidt and Shepherd completed important work in the Caltech Ludwieg Tube demonstrating that a coherent oscillation could be detected in the neck region of the flowfield. It was shown that if a Strouhal number was constructed that normalized the frequency with the slipline length, a constant Strouhal number would be observed for a range of Reynolds numbers. This finding suggests that the slipline length and its associated acoustic phenomena are responsible for a characteristic frequency in this flowfield (Schmidt 2015). Immediately, this suggests that a fundamentally different physical mechanism is at play, since the subsonic cylinder wake requires normalization by the cylinder diameter, not the slipline length.

It has been suggested these oscillatory instabilities in the neck region of the flow could create acoustic waves that propagate upstream through the subsonic dead-air region (Awasthi 2022). If such a phenomenon occurred, it would potentially create an acoustic feedback loop where instabilities would travel downstream along the sliplines, perturb the neck region, generate acoustic waves that would travel upstream through the dead-air region, and these waves would perturb the separation points causing instabilities to again generate along the slipline. Additionally, analytical attempts, based on a Rossiter-like feedback mechanism, to derive the characteristic frequencies measured in the flowfield support the idea of an acoustic feedback loop (Thasu 2022).

The primary motivation for this project was to utilize the capabilities of the Caltech Ludwieg Tube to generate steady and lengthy supersonic flow, in combination with modern schlieren imaging and spectral flowfield analysis techniques. The results from the project show evidence for an acoustic feedback loop that governs the characteristic fluctuations detected in the neck region of the flow, including the detection of upstream acoustic waves within the dead-air region. The details of these results are more carefully discussed in the following section. Additionally, the project aims to improve upon the work of Schmidt and Shepherd by creating a non-intrusive extended cylinder mount that will capture more of the test flow and generate cleaner data. A diagram of this goal is shown in Figure 5.

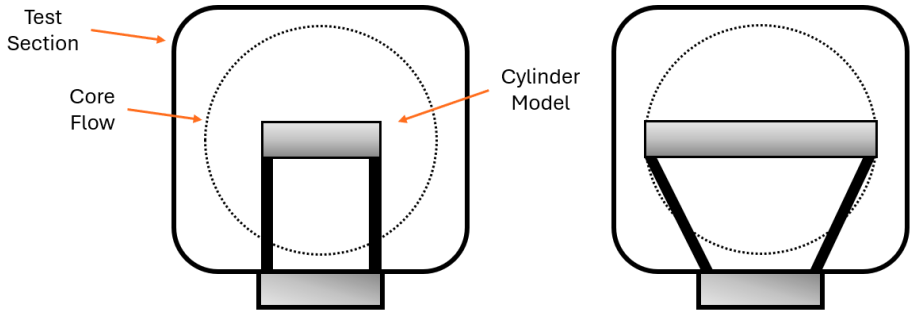


Figure 5.
Left Schmidt and Shepherd's cylinder mount from 2015
Right This project's extended cylinder mount

RESULTS

Several key results were obtained from this project. They are categorized in this discussion into flowfield-wide results and dead-air results. Flowfield-wide results are measurements and findings obtained from the imaging and SPOD analysis of the entire wake flowfield. Dead-air results are findings obtained from the application of SPOD to only the dead-air region of the flowfield.

Flowfield data were obtained experimentally using schlieren imaging, a classical optical technique that visualizes first spatial derivatives of density as variations in image intensity. Further details on the schlieren setup and image acquisition are provided in the Methods section. The resulting time-resolved images were then analyzed using spectral proper orthogonal decomposition (SPOD), which identifies coherent fluctuating structures and ranks them by their energy at each frequency. Each SPOD mode therefore has a characteristic frequency, spatial structure, and energy. SPOD was applied both to the entire measured wake and separately to the dead-air region; the complete analysis procedure is described in the Methods section.

1. FLOWFIELD-WIDE RESULTS

The most immediate flowfield-wide result obtained from this project is the successful imaging and measurement of the supersonic cylinder wake flowfield. A frame from a particular case is shown in Figure 6.

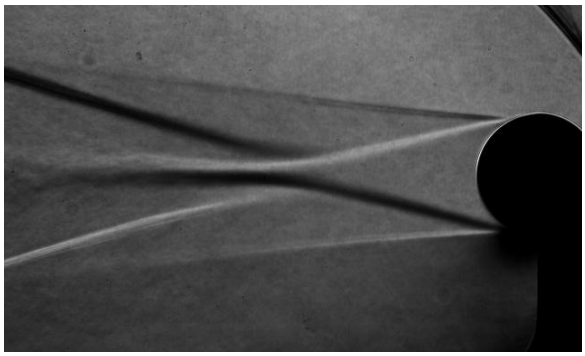


Figure 6. Single schlieren frame of the 19mm cylinder wake

A comprehensive list of the Reynolds numbers spanned by this project is listed in Table 1.

Re_D	D (mm)
$8.90E4$	19
$1.18E5$	19
$1.58E5$	19
$1.96E5$	19
$2.67E5$	44.5
$2.76E5$	19
$4.89E5$	44.5

Table 1. Test Reynolds numbers

The next crucial result was the recreation of the Strouhal number collapse originally found by Schmidt and Shepherd in 2015. To recreate this result, a Fast Fourier Transform was performed on a point in the neck region. To reduce noise, a 3x3 group of pixels were averaged to generate a single average pixel intensity over time. A Strouhal number is calculated that normalizes the detected peak frequencies with the measured slipline length. The formula for Strouhal number is shown in Equation 1.

$$St_S = \frac{fS}{u_\infty} \tag{1}$$

Where u_∞ is the freestream flow velocity, and S is the slipline length. The key finding of Schmidt and Shepherd is the existence of a constant Strouhal number for a range of Reynolds numbers. The original collapse and the collapse verified by this project are shown together in Figure 7. A similar Strouhal number of ~0.48 is seen for both studies. Error bars are generated using a Full Width at Half Maximum (FWHM) calculation of the detected peak frequencies.

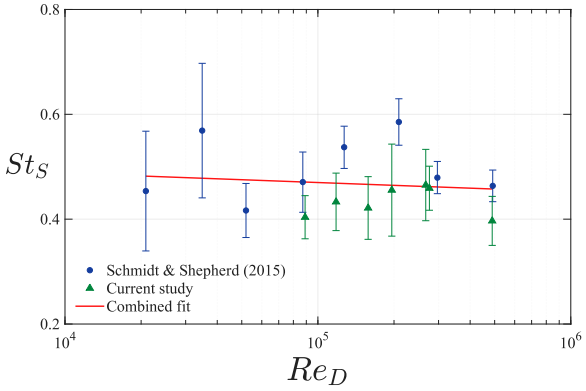


Figure 7. Strouhal number collapse

With the confirmation that the characteristic frequency was properly measured, the SPOD technique was applied to the entire flowfield. A figure that shows the frequency spectrum of this analysis for $Re_D = 1.96E4$ is shown in Figure 8.

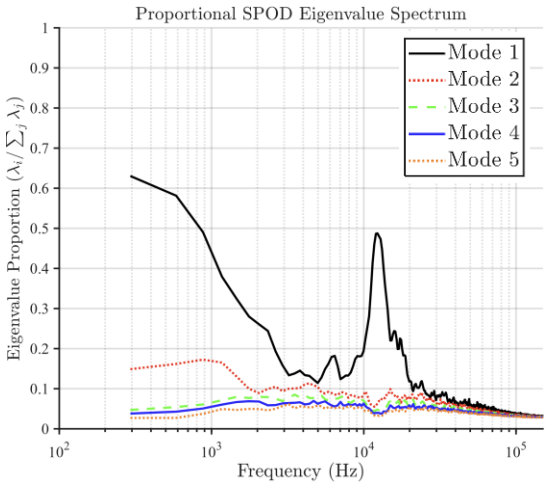


Figure 8. SPOD eigenspectrum for cylinder wake at $Re_D = 1.96E5$

The lines denote different oscillatory modes corresponding to different structures in the flow. A particular peak shows that a single oscillatory mode can represent a large amount of fluctuating behavior in the flow. This is known as low rank behavior and usually indicates the existence of an important physical phenomenon. The spatial contour plot of the dominant mode at the peaked frequency is shown in Figure 9.

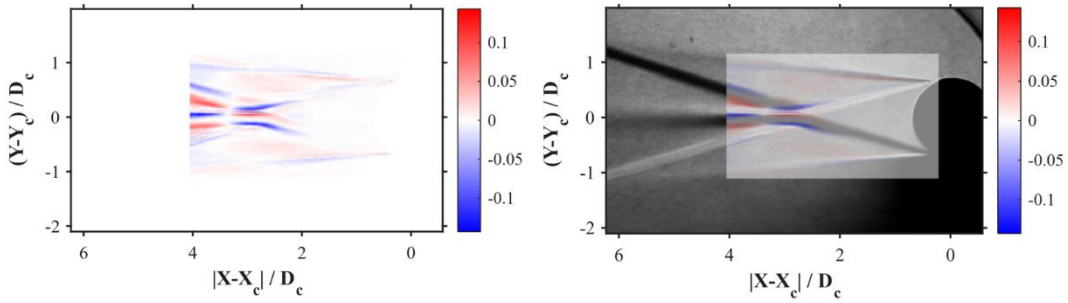


Figure 9. Mode 1 spatial plot at 13.2 kHz for $Re_D = 1.96E5$ where axes are normalized by cylinder diameters

This plot represents one of the key findings of this project. We see a very coherent structure at the exact frequency found by conventional pointwise FFT methods shown in Figure 7. The spatial plot shows a clear downstream propagation of instabilities through the sliplines. As these instabilities feed into the neck region, the characteristic collapse frequency of the flow is realized. Through the combination of SPOD techniques and recreating the original Schmidt and Shepherd findings, this project found a clear downstream mechanism responsible for the collapse frequency of this flowfield. This finding is particularly important regarding the idea of an aeroacoustic feedback loop. This SPOD structure indicates a possible mechanism for which instabilities can propagate downstream along the sliplines. More specifically, the mode suggests that the sliplines oscillate perpendicularly to the direction of the slipline itself. This instability seems to become more intense as it travels farther away from the separation point.

It is worth noting here that SPOD analysis allows the calculation of several other modes. A diagram showing the first 3 dominant modes at 3 different frequencies is shown in Figure 10.

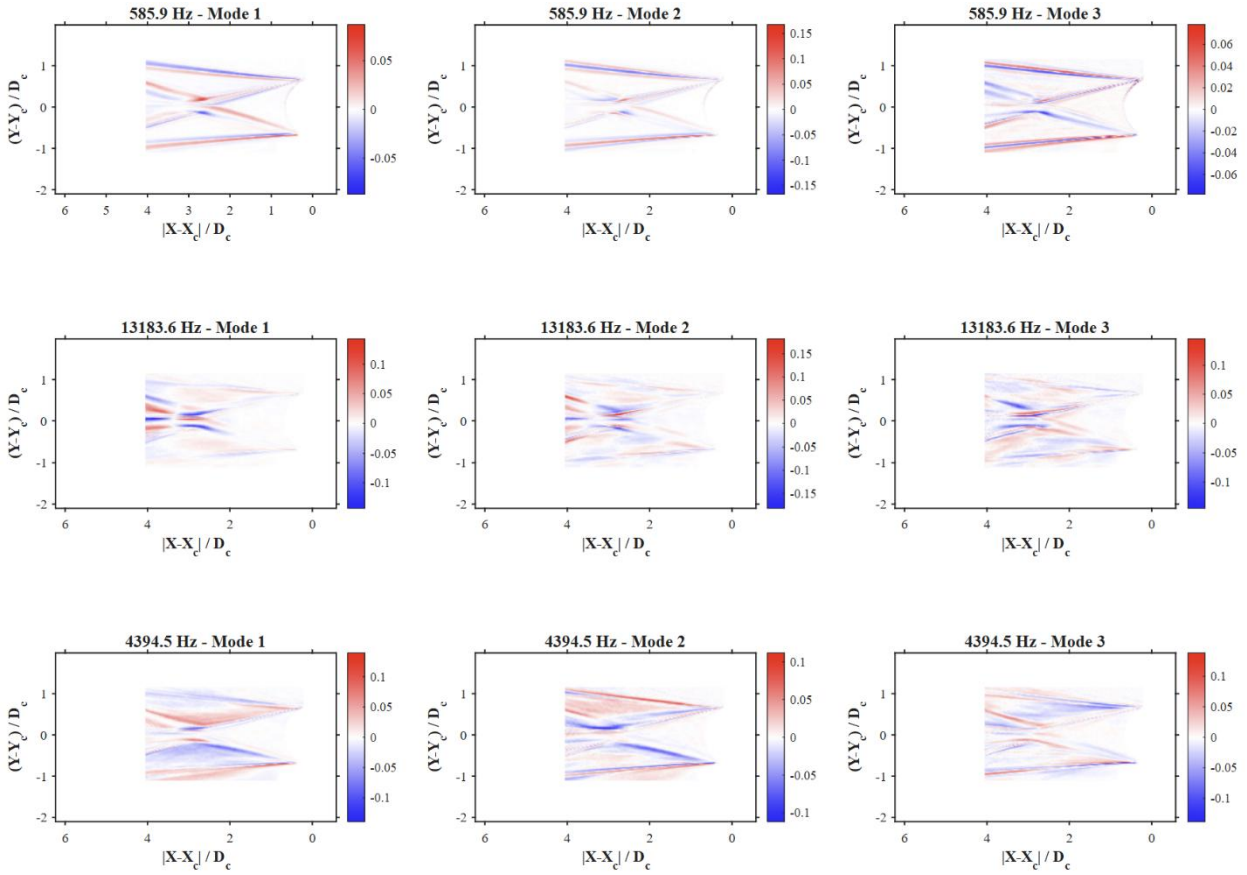


Figure 10. Top 3 dominant modes at 3 different frequencies for $Re_D = 1.96E5$

The collapse frequency structure is a behavior that was measured across a range of Reynolds numbers. If the mode 1 peak is examined across a range of Reynolds numbers in this collapse frequency range, a trend appears in the peak frequency.

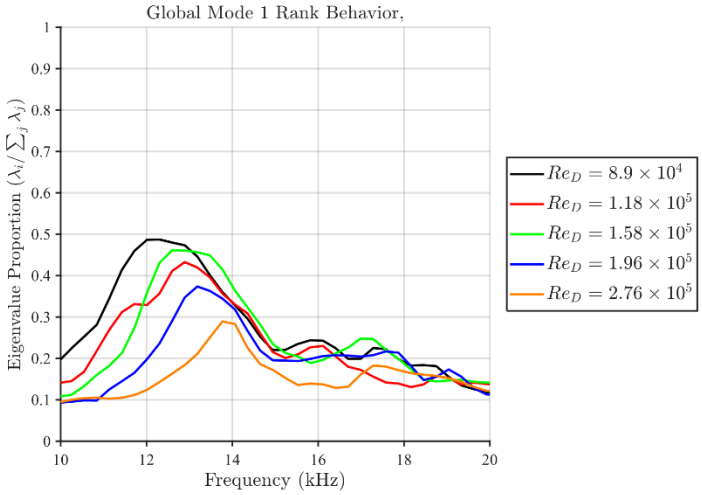


Figure 11. Mode 1 peak for range of Reynolds Numbers

As the Reynolds number increases, the peak frequency shifts higher. This supports the behavior of the constant Strouhal number. As the flow condition increases in Reynolds number, the slipline length will shrink. As a result, the characteristic frequency must increase to maintain a constant Strouhal number. This is a key result, as it allows not only the validation of the collapse frequency but the addition of spatial information to this finding as well.

2. DEAD-AIR RESULTS

The SPOD technique was also independently applied inside the dead-air region. This region presents a unique challenge. The flow in this region is very stagnant, and acoustic waves propagate in this region from all directions. Oscillations in the separation point, neck region, and sliplines all generate separate acoustic waves that create a very noisy and difficult to analyze portion of the flowfield.

This is particularly troublesome for the application of SPOD techniques, as low rank behavior will only appear if a single harmonic mode can encapsulate the flow fluctuations. While this may be possible for acoustic wave emissions from a single source, the multidirectional nature of the noise within the dead-air region makes low rank behavior nearly impossible to detect. To address these challenges, a few steps were taken. First was the adjustment of the schlieren cutoff to a vertical configuration. This allowed the optical setup to be sensitive to structures moving in the flow-wise direction. In particular, this step was taken in an attempt to measure upstream propagating structures. Second was the masking of the dataset to only apply SPOD techniques within the dead-air region. This was a choice made to avoid potentially harmonic modes within the dead-air region having to compete with more powerful modes outside of the region of interest. The eigenspectrum plot of the SPOD results from the dead-air region is shown in Figure 12.

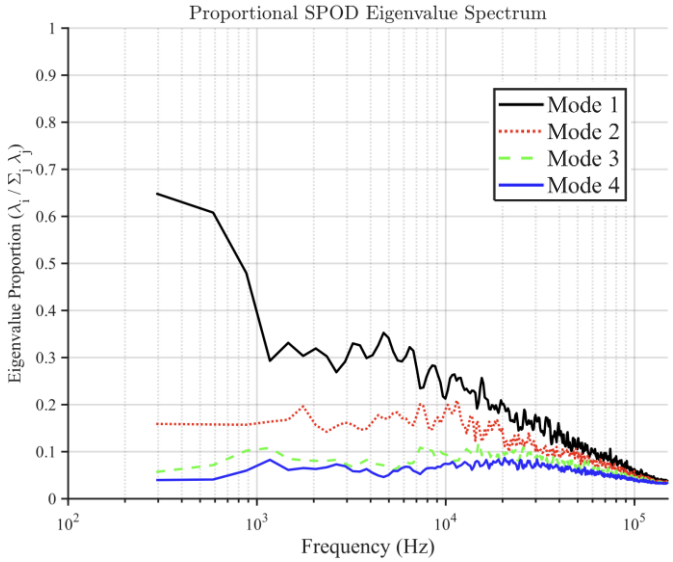


Figure 12. Dead-air eigenspectrum plot at $Re_D = 1.96E4$

Clearly the different modes are quite similar in power, and there is no discernible low rank behavior. As a result, the project utilized a frequency-driven approach. Having measured a clear characteristic peak using the flowfield-wide SPOD analysis, the same frequency was explored in the dead-air region.

We find that although the first mode is a downstream propagating acoustic wave, the second mode shows an upstream propagating acoustic wave. A contour plot of this spatial mode is shown in Figure 13.

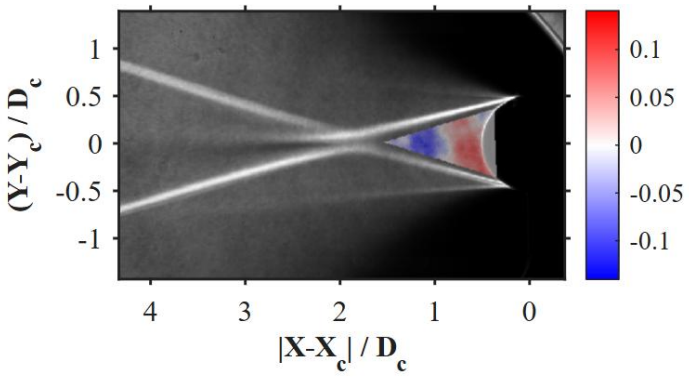


Figure 13. Upstream propagating structure found in Mode 2 at 13.2 kHz

Although the structure was detected in the second mode, the power distinction between the first and second mode becomes minimal when there is no low rank behavior. We find that acoustic waves in this region are travelling in all directions, but that these measurements are particularly sensitive to horizontal propagation owing to our choice of cutoff direction. Different phase locations of the mode illustrate this upstream movement. These stills are shown in Figure 14.

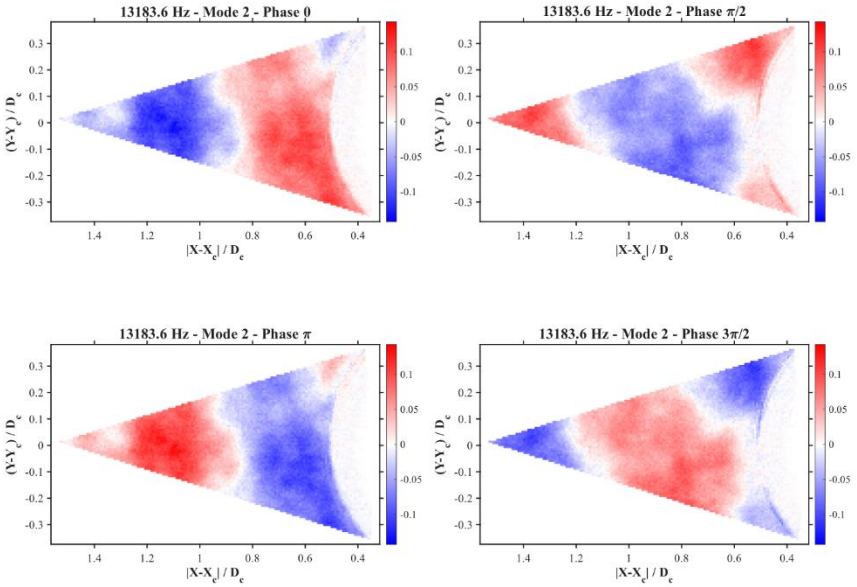


Figure 14. Phase stills of the upstream propagating mode

The analytical models supporting the existence of upstream acoustic structures rely on an assumption that the upstream waves have a wavelength approximately equal to a slipline length (Thasu 2022). Because the upstream structure seen in our SPOD results are seen across a range of frequencies, some effort was spent to measure the wavelength of the structures across a range of frequencies. The results are shown in Figure 15.

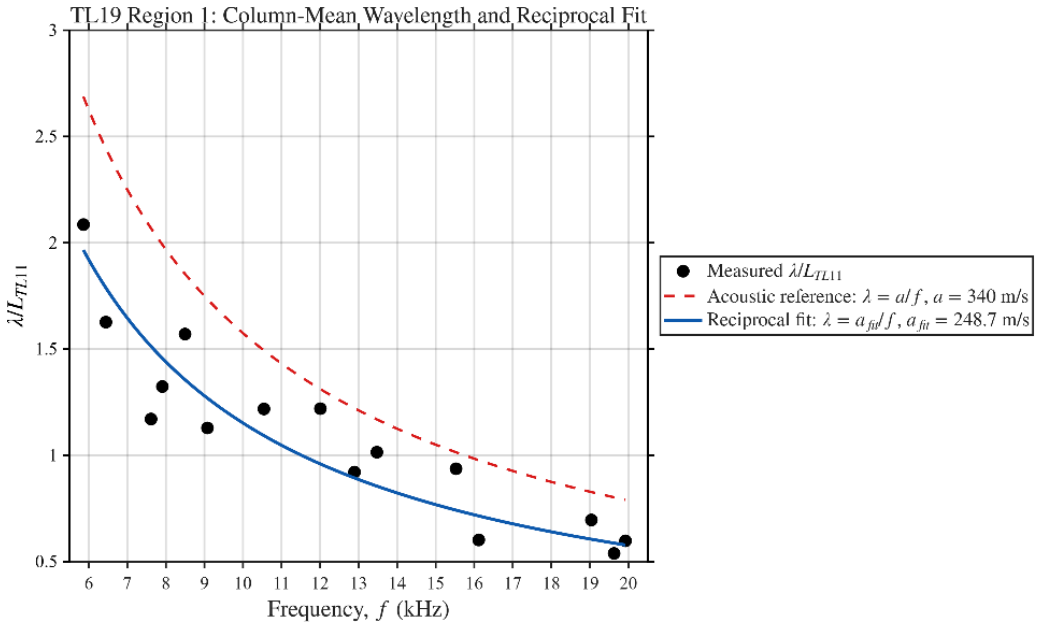


Figure 15. Measured wavelength of upstream structure over frequency

The y-axis in the plot shows the wavelength of the structure normalized by the slipline length. We can see that approximately at the collapse frequency (~13 kHz), the wavelength becomes around a slipline length. This is a very promising result. The acoustic reference shows that this wave structure follows the behavior we expect to see from an upstream acoustic structure, and that this wave has a wavelength of around a slipline length. This result strongly supports the analytical efforts that have been completed in the literature.

Taken together, the results of this project make large strides in the way of experimentally validating the analytical models offered by other researchers in this field. The measurement of upstream acoustic waves in the dead-air region is an exciting and important result and further characterizing these wave structures' properties is an important avenue for future work.

METHODS

1. CALTECH LUDWIEG TUBE

As previously mentioned, this project utilized the Caltech Ludwieg Tube to generate Mach 4 flow. The Caltech Ludwieg Tube is a blowdown facility and operates by jetting a high-pressure driver tank into a vacuumed test section and dump tank. More specifically, a piston-operated plug closes the nozzle throat until the desired fill pressure is reached. When the piston is actuated, the flow is choked and accelerated to Mach 4 through the contour nozzle and provides lengthy and steady test flow of around 60-80 milliseconds. A model of the facility is shown in Figure 16. A nozzle pressure trace is shown in Figure 17.

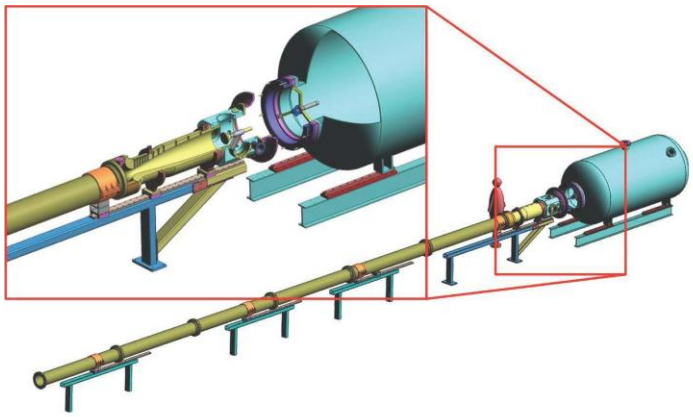


Figure 16. Model of the Caltech Ludwieg Tube facility

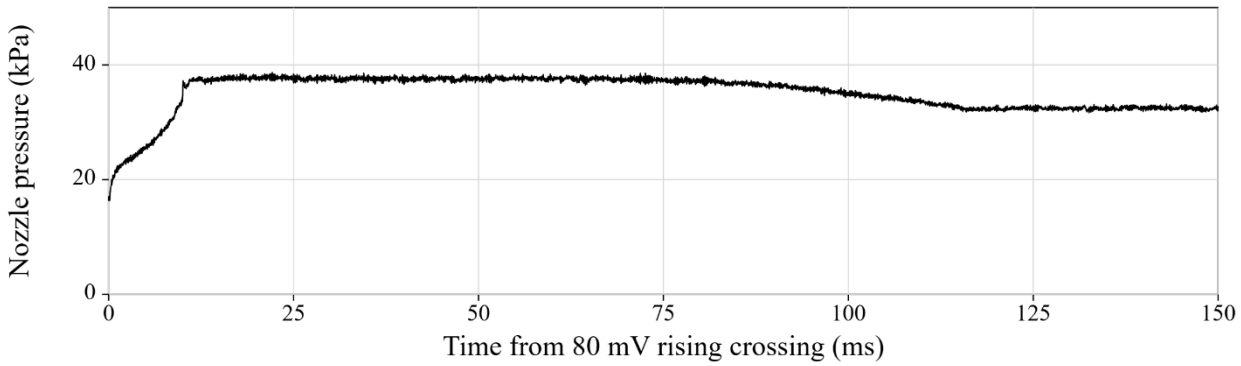


Figure 17. Ludwieg nozzle pressure trace, starting from oscilloscope trigger

In return for generating extremely quiet and long test flow, the Ludwieg Tube is unable to recreate the high-enthalpy flow conditions a supersonic or hypersonic vehicle would encounter during real flight in Earth's atmosphere. Consider the well-known equation that relates stagnation and static temperature for 1-dimensional isentropic flows.

$$\frac{T_0}{T} = 1 + \frac{\gamma - 1}{2} M^2 \tag{2}$$

Where T_0 refers to stagnation or total temperature, T refers to static temperature, γ refers to the specific heat ratio of the fluid, and M refers to the Mach number of the fluid. When the Ludwieg Tube generates Mach 4 flow, the acceleration from room temperature causes the gas to exhibit a freestream static temperature of around 70 K. As a result, this project is unable to explore the high-enthalpy chemistry that is essential to hypersonic and supersonic flow study. However, there is still a high amount of fundamental fluid mechanics that this facility can reveal, particularly with its extremely steady and lengthy test time.

A key functionality of the Ludwieg Tube is the ability to control the freestream Reynolds number by varying the upstream driver pressure. To understand how this occurs, consider the equation defining Reynolds number.

$$Re_D = \frac{\rho u_\infty D}{\mu} \tag{3}$$

Where D denotes the cylinder diameter, ρ denotes static density, u_∞ denotes flow velocity, and μ represents the dynamic viscosity of the fluid. For a particular cylinder geometry, the diameter is constant. Furthermore, because sound speed depends on temperature, the velocity of the freestream gas will not change with upstream pressure. As a result, changing the upstream pressure only varies the freestream density ρ. To understand this relationship more completely, consider the following equation governing density of an isentropic flow.

$$\rho = \rho_0 \left(1 + \frac{\gamma - 1}{2} M^2\right)^{\frac{-1}{\gamma - 1}} \tag{4}$$

By assuming that the driver section exhibits ideal gas behavior, which is a reasonable assumption for high-pressure air at room temperature, we can relate the freestream static density to the total pressure of the flow. In this case, the total pressure of the flow is equal to the driver tube fill pressure. We get the following.

$$\rho = \frac{P_0}{RT_0} \left(1 + \frac{\gamma - 1}{2} M^2\right)^{\frac{-1}{\gamma - 1}} \tag{5}$$

Substituting this equation into the definition of Reynolds number yields the following relationships.

$$Re_D = \frac{P_0 u_\infty D}{RT_0 \mu} \left(1 + \frac{\gamma - 1}{2} M^2\right)^{\frac{-1}{\gamma - 1}} \tag{6}$$

$$P_0 = \frac{RT_0 \mu Re_D}{u_\infty D} \left(1 + \frac{\gamma - 1}{2} M^2\right)^{\frac{1}{\gamma - 1}} \tag{7}$$

Equation 7 allows us to calculate a desired upstream fill pressure for a desired Reynolds number condition. In the case of the Ludwieg Tube, the total temperature is approximately room temperature. Using this relationship, a test matrix was calculated which is shown in Table 2.

Re_D	D (mm)	P_0 (kPa)
$8.90E4$	19	103
$1.18E5$	19	136
$1.58E5$	19	183
$1.96E5$	19	227
$2.67E5$	44.5	132
$2.76E5$	19	319
$4.89E5$	44.5	242

Table 2. Ludwieg Tube test matrix

To validate a steady Mach 4 flow, this project also undertook a Machline experiment. Small strips of tape were placed on the contour nozzle to generate weak shock lines into the test section. An image of the tape is shown in Figure 18.



Figure 18. Tape placement on the contour nozzle

The measured Machlines both validated the schlieren system and the steady Mach 4 flow. A frame from the dataset is shown in Figure 19.

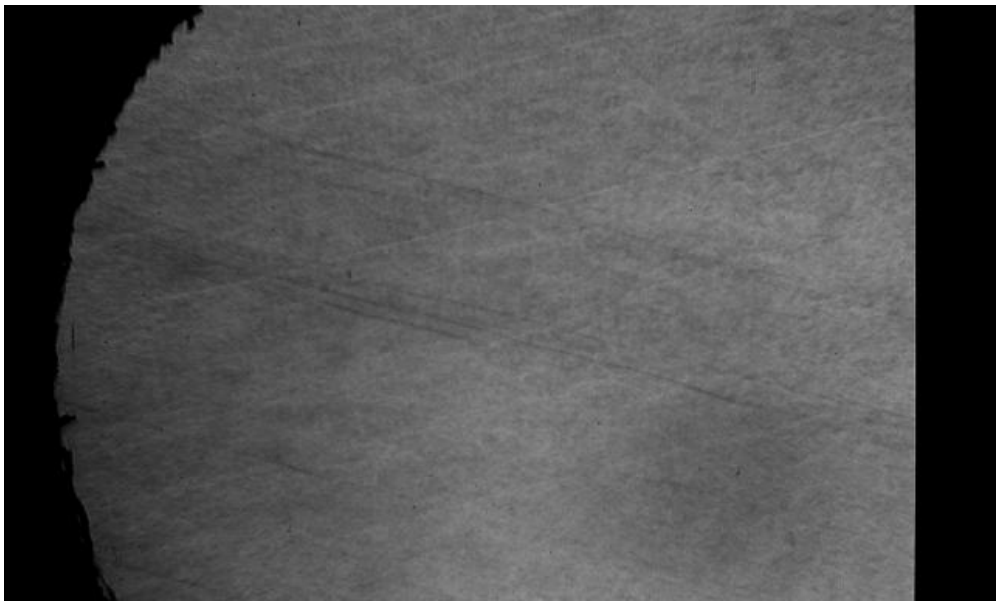


Figure 19. Single frame image of the Machlines

The digitally measured Machlines have an angle of ∼14.5° while the theoretical Mach angle is ∼14.4°. This verifies both steady Mach 4 flow and the workflow of schlieren measurement and analysis.

2. MODEL DESIGN & STRUCTURAL VALIDATION

The design of the cylinder model required the consideration of multiple design constraints and objectives. Listed below are the considerations taken to ensure the design of a successful model.

1. Model must secure a cylinder in the center of the test flow (should not be secured lower or higher than the center plane of the nozzle)
2. Model stings or supporting structure must minimally incur on the test section flow
3. Model stings or supporting structure and cylinder must not deform noticeably
4. Model must be easy to manage in the laboratory setting

The final design of the model is shown in Figure 20. The design secures the cylinder through 2 stings that comprise the supporting structure. The stings are connected to a yaw plate, which is connected to a flange that attaches directly to the Ludwieg Tube test section. The entire assembly is constructed from 6061 aluminum, except for the 19mm cylinder itself which is constructed from 303 steel.

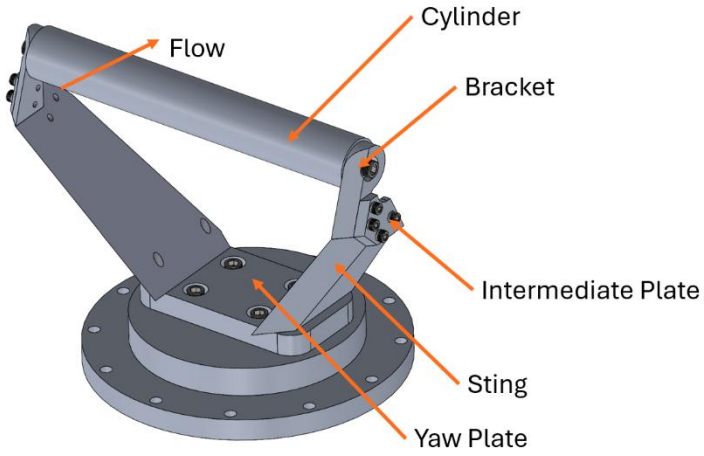


Figure 20. Isometric view of the cylinder model

The stings, brackets, and intermediate plate present an angled face to the oncoming flow, which helps avoid the generation of spurious shockwaves into the core flow. The yaw plate and its associated screws have tolerances that allow the plate to slide small amounts over the flange. Using this the model was aligned with the optical setup and the oncoming flow.

To ensure that the cylinders could be easily exchanged in the laboratory, the model was designed such that the cylinder and bracket components could be removed from a previously aligned sting assembly. This linkage represented an area of important consideration as it was a highly stressed component of the assembly. The final design allows the bracket component to rest in a slot on the sting component. The two pieces are then connected securely through the intermediate plate. The linkage is shown through a series of images in Figure 21.

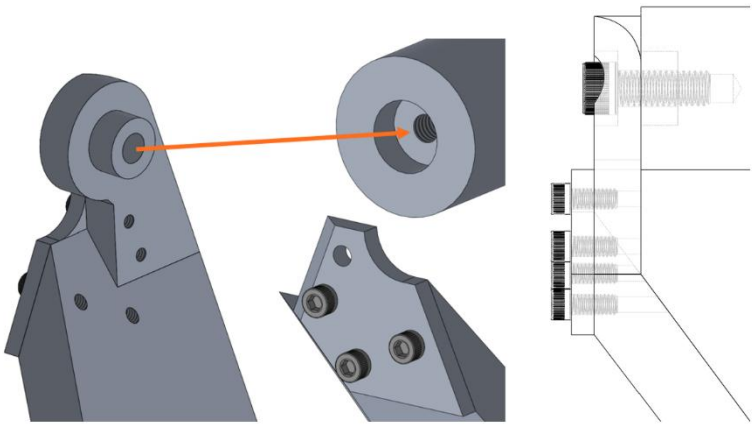


Figure 21. Images of the cylinder linkage

To ensure that this design could withstand both the freestream pressure force of the Ludwieg Tube's Mach 4 flow, and the impulsive force of a sudden supersonic startup, this project utilized the static structural simulation software included with SolidWorks. The simulation was set up by applying a static force load on the cylinder surface, and holding the bottom of the stings fixed. In addition, the screws were individually simulated to ensure that the design would not shear the screws during operation. The mesh was refined in regions nearing and inside the screw holes. A diagram showing the setup of the static simulation is shown in Figure 22. An earlier simulation used incorrect preload values for the screws, resulting in high axial stress in the screws and surrounding structure. This was fixed by using the standard preload datasheets to apply appropriate preload values in the Solidworks simulation software.

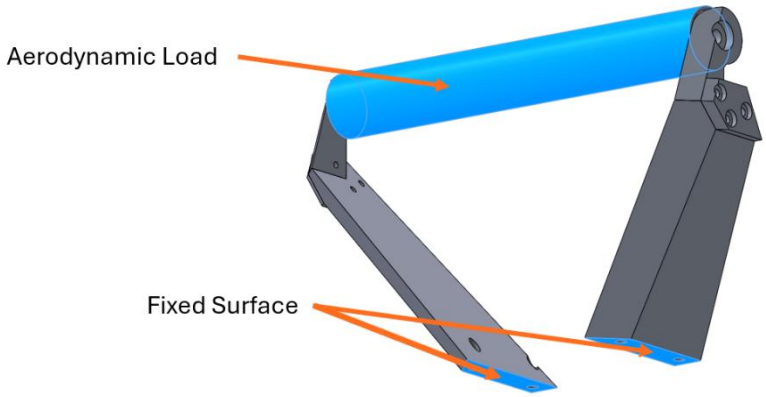


Figure 22. Diagram of the structural simulation setup

The aerodynamic load was determined using a drag coefficient calculation. With a known upstream driver pressure (determined from the highest pressure Reynolds number condition required), the freestream static pressure can be calculated from equation 8.

$$P = P_0 \left(1 + \frac{\gamma - 1}{2} M^2\right)^{\frac{-\gamma}{\gamma - 1}} \tag{8}$$

With the freestream pressure, the freestream dynamic pressure is calculated using equation 9.

$$q_\infty = \frac{\gamma}{2} P M^2 = \frac{1}{2} \rho v^2 \tag{9}$$

The front-facing area of the cylinder can be calculated by multiplying the length of the cylinder with its diameter. With the freestream dynamic pressure, coefficient of drag of a supersonic cylinder, and front facing area, the drag force for a particular flow condition can be calculated using equation 10.

$$F_D = q_\infty C_D A \tag{10}$$

The drag forces were calculated as the highest-pressure cases at each diameter. Additionally, the forces were multiplied by 2 to ensure the model could survive the startup impulse. A drag coefficient of 1.3 was used (Gowen 1953).

Simulation results showed that stress concentrations would occur at the screw holes in the linkages. A contour plot of a simulation for the 44.5mm cylinder is shown in Figure 23.

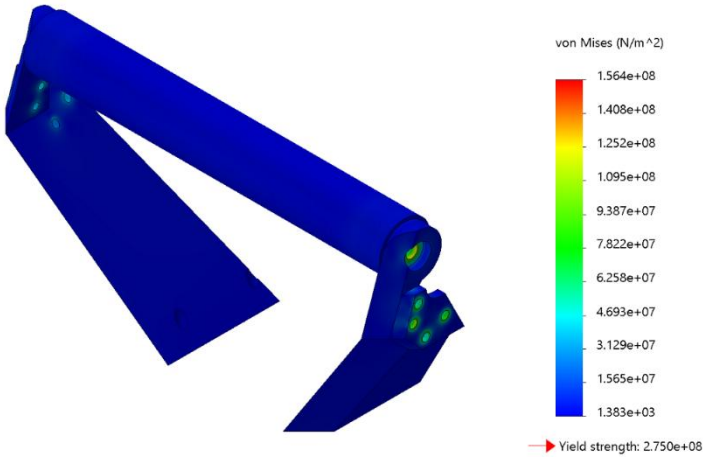


Figure 23. Stress contour plot of the 44.5mm cylinder simulation

3. SCHLIEREN IMAGING

Having established the methods for generating supersonic flow and validating the cylinder model, the focus now shifts to imaging and measuring the flowfield. The technique utilized by this project is known as schlieren imaging and is a traditional and well understood technique. The information presented in this section is brief and is only introductory. A more complete discussion can be found in the famous book written by Settles (Settles 2001).

Schlieren is a technique that images 1st derivative density gradients in a medium as an image intensity. It can accomplish this by taking advantage of the fact that refractive index is dependent on the density of a material.

The imaging technique is implemented by generating a collimated light beam and sending through a test medium. In the case of this project, a collimated light beam was sent through the Ludwieg Tube test section. As density gradients appear in the medium from shockwaves and expansions, the local refractive index changes and deflects rays of light from the collimated path. The beam is focused down to a point, where a knife-edge is placed. The idea is that stray rays will be disproportionately affected by the knife-edge and cause a darkening or lightening of the image in that local area. The result is a powerful technique that allows the imaging of shock structures in a flowfield.

This project focuses on the fluctuations in the wake flowfield, which does not necessitate quantitative knowledge of the density in the flowfield. It is possible, however, to perform a form of integration across a schlieren dataset to obtain precise density information at each point in the flow. Such a technique is known as "quantitative schlieren," which requires a much more precise and well-tuned schlieren setup than the one utilized in this project. A diagram of a typical schlieren setup is shown in Figure 24.

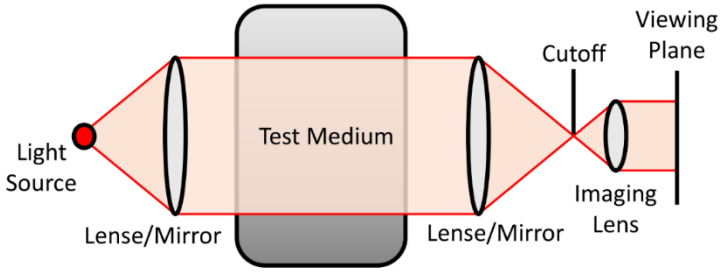


Figure 24. Diagram of a typical schlieren imaging setup

More specifically, this project utilized a setup known as a z-type schlieren. This type of setup allows for a very long optical path (which increases the sensitivity of the setup) while being able to fit in tight laboratory settings. A diagram of a z-type schlieren setup is shown in Figure 25.

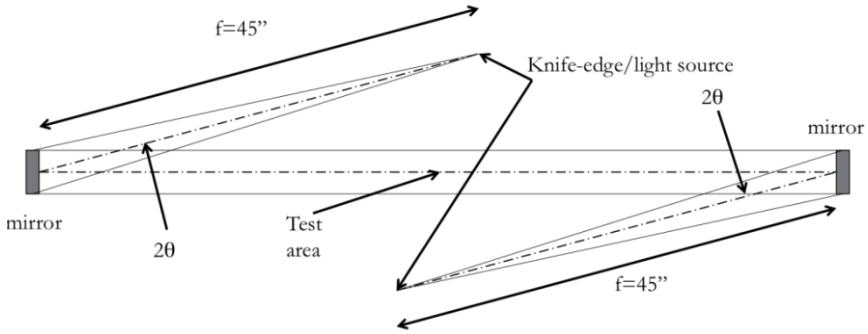


Figure 25. Diagram of a z-type schlieren setup

Significant effort was also expended to analyze the effects of varying cutoff direction and intensity. Starting with a horizontal cutoff, the effects of varying the intensity of the cutoff were analyzed. The results are shown in Figure 26. The efforts were quantified by utilizing the Phantom TMX pixel intensity readouts. An approximate average pixel intensity was recorded using the wind-off image.

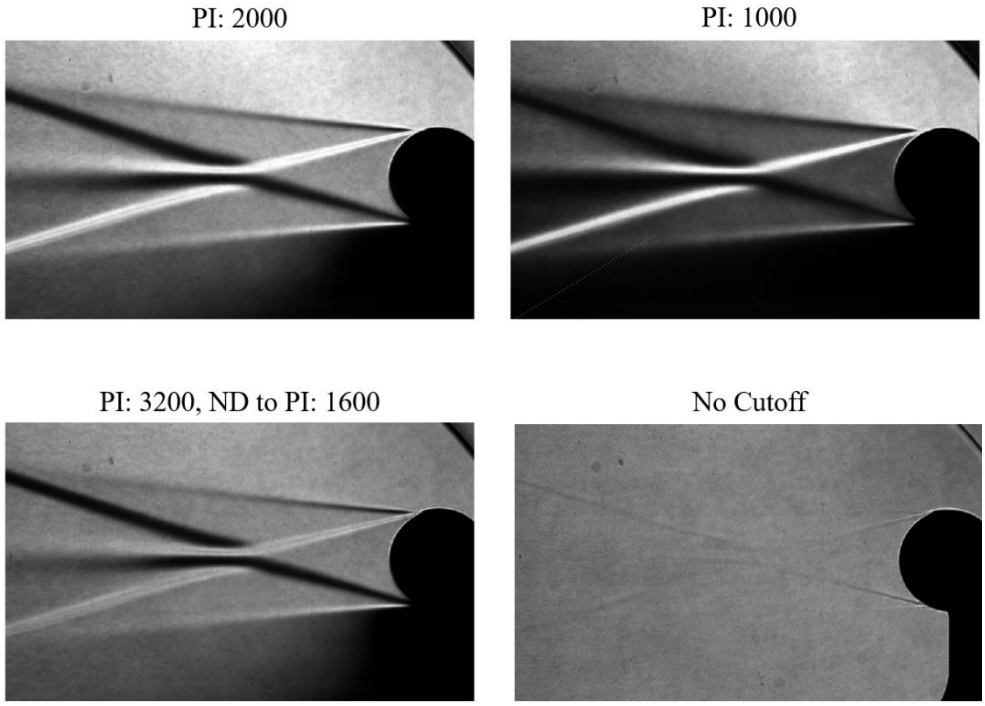


Figure 26. Effect of varying cutoff intensity where PI indicates pixel intensity

To ensure the best balance between the dark and light intensities on the image, PI 3200, ND to PI 1600 was chosen for all the shots. ND refers to a neutral density filter. This setting effectively lowers the sensitivity of the schlieren setup but brings the average pixel intensity into the middle range of the camera's intensity output.

Additionally, the direction of the cutoff was adjusted to attempt to image flow-wise gradients. An extremely aggressive vertical cutoff was used to resolve the upstream acoustic structures found in the dead-air region. An image from this setting is shown in Figure 27.

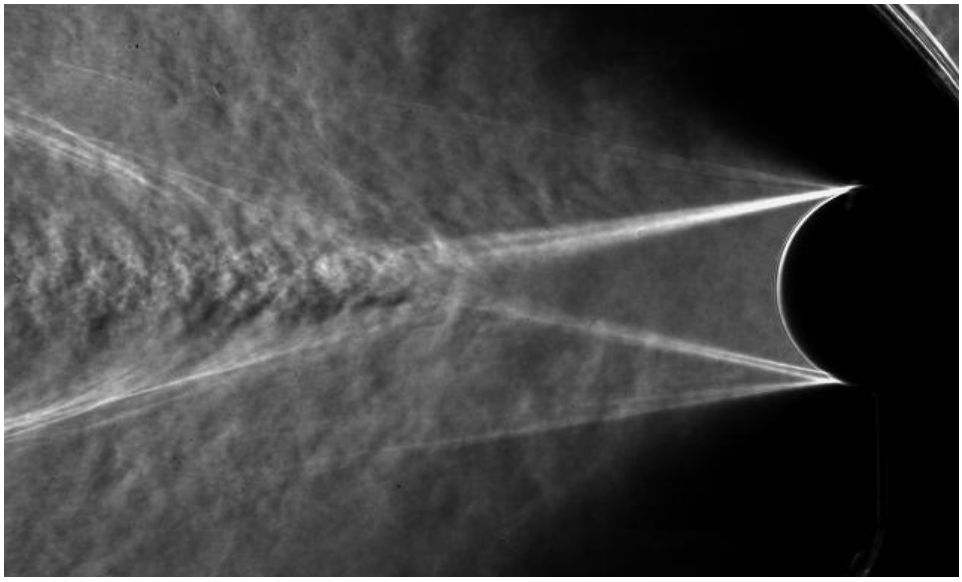


Figure 27. Frame from a PI: 1000 vertical cutoff setting

4. PROPER ORTHOGONAL DECOMPOSITION

Proper Orthogonal Decomposition (POD) forms the basis of the primary method of flowfield analysis used in this project known as Spectral Proper Orthogonal Decomposition (SPOD). The development and use of these techniques is an incredibly rich field itself and therefore is not conclusively represented in this report. Instead of exhaustively demonstrating the mathematical derivation of this method, this report will describe the general steps of implementing the method and understanding the results. A more detailed discussion of both POD and SPOD can be found in a review written by Schmidt and Colonius (Schmidt 2020).

To begin with, it is important to understand the goal of a technique such as POD. Schlieren datasets can be thought of as an intensity that depends on space and time. In other words, the pixel location and the frame number. If we denote the intensity dataset as $I(x, y, t)$, we can compute a mean image. This is done by computing the time averaged intensity for each pixel. The mean image is denoted as $\bar{I}(x, y)$. This image can be subtracted from each frame of the original dataset, leaving what is known as the fluctuating component of the schlieren dataset. This is denoted as $I'(x, y, t)$.

$$I'(x, y, t) = I(x, y, t) - \bar{I}(x, y) \tag{11}$$

This fluctuating component is responsible for the part of the dataset that changes with time. The central objective behind the POD technique is to decompose these fluctuations as a series of modes. Consider equation 12.

$$I'(x, y, t) = \sum_{i=1}^{r} a_i(t)\phi(x, y) \tag{12}$$

Where r represents the number of modes computed, $a_i(t)$ denotes the time variance coefficient, and $\phi(x, y)$ represents the spatial component. Immediately, the power behind this technique is clear. POD allows the categorization of sometimes unintelligible fluctuating flow physics into clear modes. Each mode has a time variance coefficient that describes how the mode fluctuates in time, and a spatial component that describes the location of the fluctuating behavior. Additionally, one could apply rudimentary spectral analysis techniques to the time variance coefficient to understand the coherence of a particular mode. In general, the more modes are summed, the closer the fluctuating component is to the real dataset.

Now that the fundamental goal of POD is understood, the numerical implementation of the technique is discussed. We start with an intensity dataset and isolate the fluctuating component.

$$I'(x, y, t) = I(x, y, t) - \bar{I}(x, y) \tag{13}$$

For every frame t_k a column-wise vector is constructed containing all the pixels in that frame. In other words, each frame is restructured such that the pixels are organized into a column, not a 2-dimensional matrix. For a particular frame we can construct x_k.

$$x_k = [I'_1(t_k) \dots I'_m(t_k)]^T \tag{14}$$

Here $m = n_x \times n_y$, where n_x and n_y represent the number of pixels in the x and y direction of the image. Therefore m represents the total number of pixels in each frame. Each of these vectorized frames can be concatenated into a matrix X that encodes the entire schlieren dataset into a single 2-dimensional matrix.

$$X = [x_1 \dots x_N] \tag{15}$$

Here N denotes the total number of frames in the dataset. To perform a version of the POD technique known as the Method of Snapshots, we then form a correlation matrix C.

$$C = X^T X \tag{16}$$

The Method of Snapshots works by comparing the dataset frame by frame. An alternative method known as the Direct Method forms the correlation matrix as $C = XX^T$. This has the effect of comparing the dataset pixel to pixel instead of frame to frame. Given that the next step is to compute an eigenvalue problem with the correlation matrix, one would prefer the method with the smallest matrix dimensions. It is usually the case that $N < m$, or there are fewer frames than there are pixels in a frame. As such the Method of Snapshots is usually preferred and is the focus of this report. As mentioned, the next step is to solve the eigenvalue problem with the correlation matrix.

$$CV = \lambda V \tag{17}$$

$$\phi_i = \frac{1}{\sqrt{\lambda_i}} X V_i \tag{18}$$

$$a_i(t_k) = \sqrt{\lambda_i} V_{ki} \tag{19}$$

Equations 18 and 19 show how a particular spatial mode and time variance coefficient can be calculated from the results of the eigenvalue problem. A few key properties of the POD technique should be noted here.

1. One can only compute N modes from a dataset, due to the constraints of the eigenvalue problem.
2. ϕ_i has the same dimensions as x_k meaning the display of a spatial mode requires the "unfolding" of the vector into a rectangular dataset.
3. a_i has the dimension of $N \times 1$, so it maps the progression of a particular mode through time
4. The matrix multiplication $\phi_i a_i^T$ yields a matrix with the same dimensions as X, and allows one to view the mode as a movie

To further demonstrate this technique, this project undertook a miniature investigation on an under-expanded supersonic jet. This is a canonical compressible flowfield and provided a useful test case to understand these techniques. The jet was created using a traditional lab duster and was set up

inside the Caltech Ludwieg Tube test section. A schlieren dataset was collected at 200,000 frames per second. A mean image of the video is shown in Figure 28.

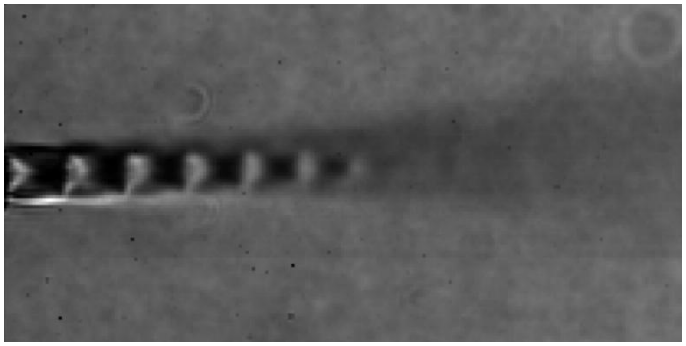


Figure 28. Mean image of under-expanded jet schlieren

Shown clearly in the mean image is the Mach diamonds as the flow expands, shocks, and expands. As the flow continues downstream, the field begins to transition to an alternating unsteady shedding behavior.

When POD is applied to this dataset, the first piece of information that we analyze is the relative distribution of "power" across the different modes. This information is presented in Figure 29.

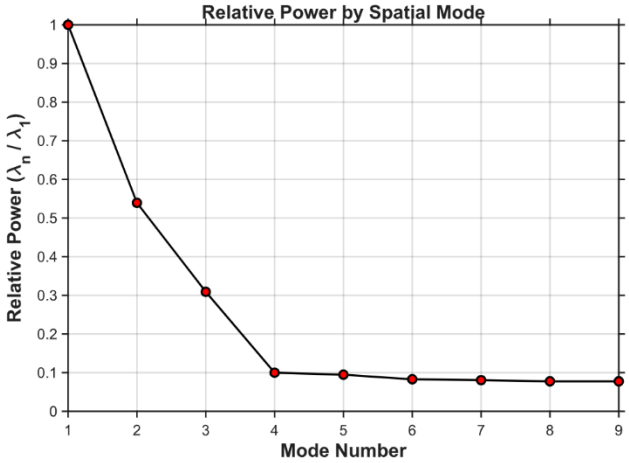


Figure 29. Relative power distribution across jet POD modes

In POD, the relative power distribution is encoded into the magnitudes of the eigenvalues calculated. A larger magnitude indicates that a particular mode comprises more of the fluctuating component of the flowfield than others. As this plot indicates, mode 1 comprises most of the flow field's fluctuations. In POD, it is ideal to see that the power is mostly distributed amongst the first few modes. This is not the case in SPOD, where single mode domination is desired. One can also see that beyond a certain point, solving for more modes does not yield any helpful results.

We can visualize the dominant mode by extracting its associated spatial component and plotting it as a contour plot. To reiterate, the spatial plot shows where these fluctuations are occurring in the flow. A color contour plot of the mode 1 spatial component is shown in Figure 30.

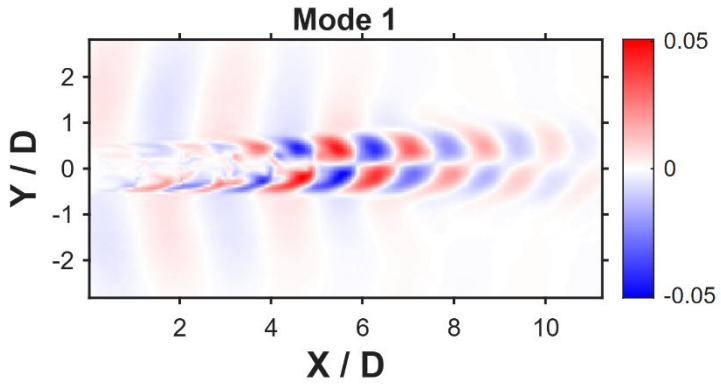


Figure 30. Spatial component plot for mode 1

Much can be understood from this plot alone. The most striking feature is the visibility of the alternating shedding structures as viscosity effects begin to contaminate the shock diamond structure. Additionally, closer to the nozzle exit there is almost no clean alternating structure. This indicates that the Mach diamond structure is somewhat stationary and very steady. The POD technique only carefully picks up on the fluctuating behavior downstream of the steady shock structure. A similar result from literature is shown in Figure 31.

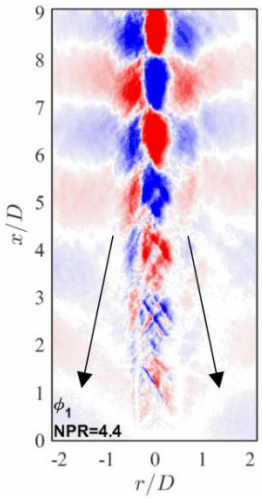


Figure 31. First mode from another supersonic jet POD analysis (Price 2020)

Lastly, we can perform some basic spectral analysis on this mode's associated time variance coefficient to understand the coherency of this mode. For a supersonic jet there exists a screech frequency at around 50 kHz. However, this screech frequency is dependent on the jet's Mach number and gas composition, both of which are not precisely known. Therefore, we can only look for an order of magnitude agreement. After generating a power spectral density plot using a Hanning Window and Welch's Method, we see a clear peak near 70 kHz for this mode. The PSD plot is shown in Figure 32.

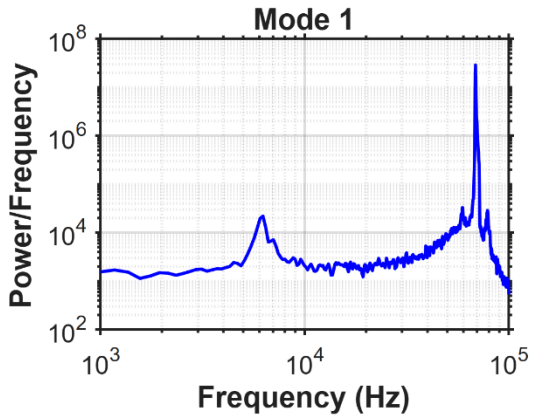


Figure 32. Mode 1 power spectral density plot

The strong peak implies that the fluctuating mode 1 is not only a dominant mode in terms of representing a large proportion of the fluctuating component of the flow, but that it is also an extremely coherent mode. This may indicate a physical phenomenon that is occurring in the flow. In the case of a supersonic jet, the downstream shedding behavior occurring at the screech frequency is a well understood and expected result.

These results help demonstrate the ability of POD to decompose and quantify the behavior of a flowfield. When trying to understand the oscillatory behavior in cylinder wake flow, methods built on the POD technique are very helpful, as they give frequency and spatial information together.

5. SPECTRAL PROPER ORTHOGONAL DECOMPOSITION

Spectral Proper Orthogonal Decomposition (SPOD) is a technique that builds on POD by enforcing every mode to exhibit harmonic behavior. To understand why one might do this, it is important to address a few important weaknesses in the POD technique.

The first is the grouping of unrelated physical phenomena. The distinction between different modes in POD is driven by the properties of solving an eigenvalue problem. That is, the POD technique only ensures that each mode is orthogonal to the others, or linearly independent. Of course, this idea of orthogonality is only with respect to the correlation matrix, not the dataset itself. The issue is that occasionally a flowfield may contain very different physical phenomena that are not properly orthogonal. As a result, the POD algorithm may output a mode that is a mix of multiple physical phenomena. This makes it exceedingly difficult to make deductions about the gasdynamics occurring in the flowfield. A side effect of this issue is also a time variance coefficient that has multiple peak frequencies or does not exhibit any coherency.

A solution to this issue is the SPOD technique, which enforces every mode to be harmonic, in addition to orthogonal. The idea is that by enforcing harmonic behavior, the algorithm should be able to isolate different physical phenomena more effectively (Schmidt 2020).

This technique begins by converting the schlieren dataset into a 2-dimensional matrix in the same way as the POD algorithm. The result set should have dimensions $M \times N_t$ where M represents the number of pixels in a frame, and N_t represents the number of frames in the dataset.

Keep in mind that N_t represents a time dimension in this matrix. The data is then segmented along this dimension using a Welch's Method scheme. Using blocks containing N_{FFT} snapshots, typically with a 50% overlap, the number of blocks is calculated as the following.

$$N_{blk} = \frac{N_t - N_{ovlp}}{N_{FFT} - N_{ovlp}} \tag{20}$$

Where N_{blk} denotes the number of blocks and N_{ovlp} represents the number of overlapped frames between blocks. To each of the blocks, a Hamming window is applied (a version of the Hanning window) to reduce segmenting noise. For each pixel, which occupies a row of the matrix, a 1-dimensional Fast Fourier Transform is performed. This effectively changes the time dimension of the matrix to a frequency dimension.

The segments can then be concatenated such that a 3-dimensional matrix with dimensions $M \times N_f \times N_{segments}$ where $N_f = N_t$ but represents the frequency dimension. If a particular column is selected from this matrix at a particular N_f the dataset encodes a specific frequency. A diagram that illustrates this method is shown in Figure 33.

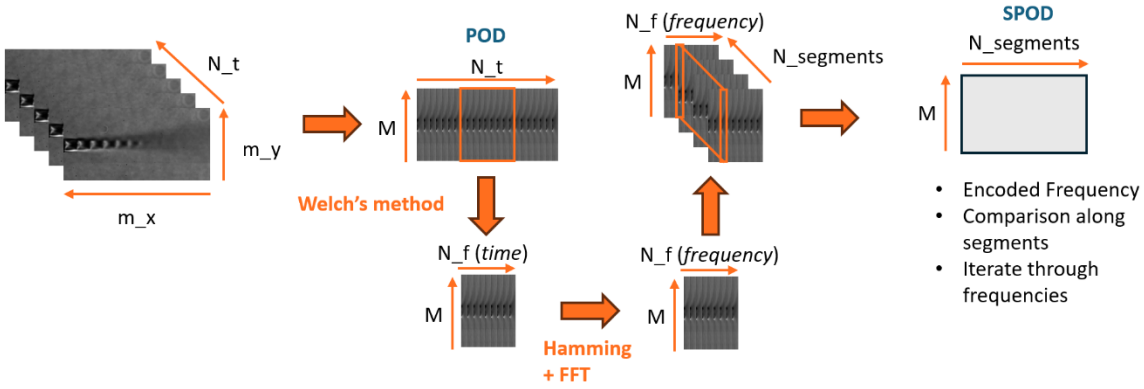


Figure 33. Diagram of the SPOD technique

This data set with dimensions $M \times N_{segments}$ encodes a specific frequency. If the POD technique is applied to this matrix, every mode that is computed will necessarily fluctuate at this encoded frequency. To compute this, a Cross-Spectral Density (CSD) matrix is computed.

$$\hat{C} = \frac{1}{N_{blk} - 1} \hat{Q}^H \hat{Q} \tag{21}$$

Where $\hat{Q}$ represents the extracted dataset. The eigenvalue problem is solved by the CSD matrix. The eigenvectors, denoted as $\hat{\psi}$ hold the information of the spatial modes at that frequency. Equation 22 details how the modes can be retrieved.

$$\hat{\phi} = \hat{Q}\hat{\psi} \tag{22}$$

A key property of the SPOD technique that differs from the POD technique is that each pixel in the spatial modes now encodes phase and amplitude information. This is because the Fast Fourier Transform leaves imaginary values in each pixel location. A way to understand this is to see the information held in each pixel as represented in equation 23.

$$\hat{\phi}(x,y) = \left|\hat{\phi}(x,y)\right| e^{i\theta(x,y)} \tag{23}$$

Where $\left|\hat{\phi}(x,y)\right|$ encodes the amplitude and $\theta(x,y)$ encodes the phase information. When we multiply the pixel value with the Euler identity to retrieve the propagation of a particular pixel in time, we get the following.

$$Re\left(\left|\hat{\phi}(x,y)\right| e^{i\theta(x,y)} \cdot e^{2\pi f t}\right) \tag{24}$$

$$Re\left(\left|\hat{\phi}(x,y)\right| e^{i(2\pi f t + \theta(x,y))}\right) = \left|\hat{\phi}(x,y)\right| cos(2\pi f t + \theta(x,y)) \tag{25}$$

Equation 25 demonstrates how the result of an SPOD analysis necessarily encodes a harmonic value into each pixel. In other words, the mode can be represented as a cosine wave function at each pixel.

Returning to our example of an under-expanded jet, an SPOD analysis reveals the following eigenspectrum plot.

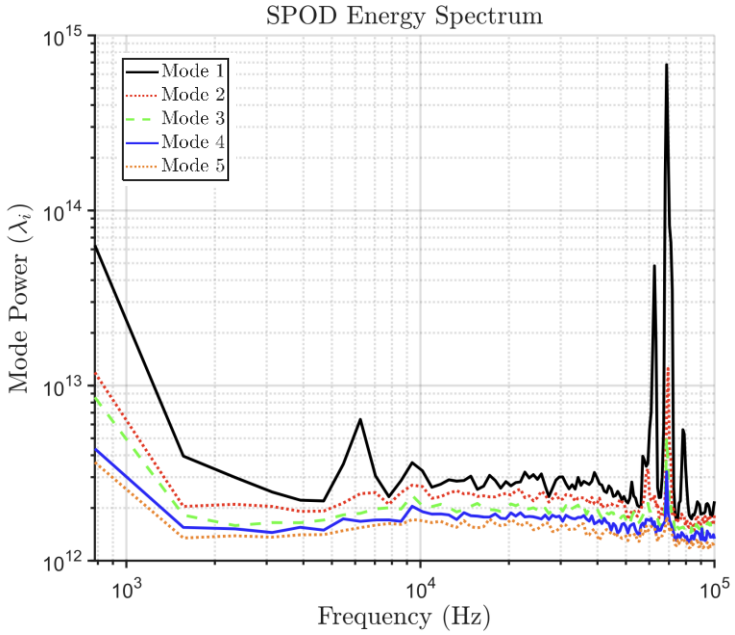


Figure 34. Jet SPOD eigenspectrum plot

This plot is one of the key results of SPOD analysis. The x-axis shows the frequencies that were iterated through. If a vertical line is drawn at a particular frequency, the heights of the lines give an indication of the modal power at this frequency. This is identical to the POD modal distribution

plot. In general, one is looking for a frequency where mode 1 accumulates a large amount of power relative to the lower order modes. This indicates that a particular harmonic mode can represent a disproportionately large amount of fluctuation in the dataset. In the case of the supersonic jet, we see this behavior at exactly the screech frequency of the jet: ~70 kHz. This is known as low rank behavior.

One can then plot the dominant mode in this frequency. A contour plot of mode 1 at the low rank frequency is shown in Figure 35.

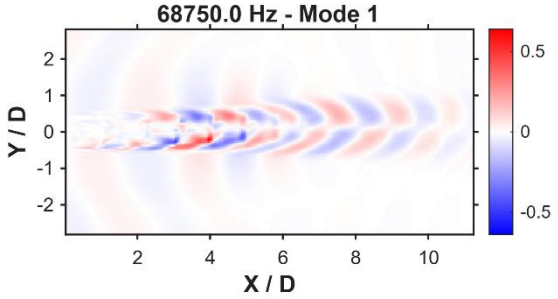


Figure 35. Dominant mode 1 contour plot

The plot shows the same alternating shedding behavior that was detected during the POD analysis. The advantage with SPOD however, is that by forcing harmonicity we can isolate this physical phenomenon more clearly. When encountering flowfields with many different physical phenomena, having the ability to sort by frequency can sometimes help with categorizing the behaviors in different regions of the flow.

Another property of SPOD analysis is the low rank behavior will only occur if the mode can characterize a large amount of the flow's fluctuations. A way to help highlight specific flow features as low rank behavior is to mask those regions separately and perform SPOD on each region individually. This helps promote structures in different regions of the flow that may be experiencing significantly different flow conditions. A map of the masks applied for the cylinder wake analysis is shown in Figure 36.

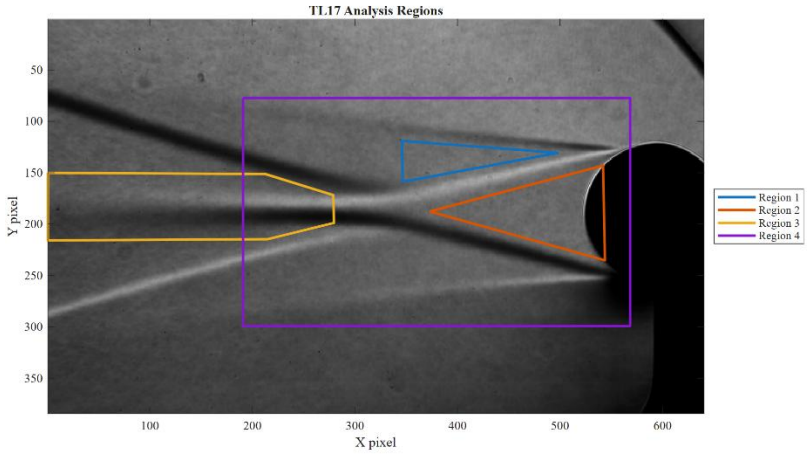


Figure 36. Region masks used for cylinder wake analysis

An additional technique that assisted our SPOD analysis was to normalize the pixel values with respect to a particular frame's average pixel intensity for each frame. This helped highlight the fluctuating component and eradicate issues in our imaging setup that cause flickering. The flickering was harmonic and would show up as peaks in our SPOD analysis.

CONCLUSION

This project represents a few key advances in the understanding of supersonic cylinder wake flow. The first is the uncovering of the downstream slipline oscillations occurring at the characteristic collapse frequency of the flowfield. The second is the measurement of upstream acoustic structures in the dead-air region. These results are not complete but represent steps towards experimentally validating the aeroacoustic feedback loop that has been suggested in literature. Potential next steps are offered below.

- Measure upstream acoustic structures for a range of Reynolds numbers, and compare their wavelength behavior with the expected characteristic frequency.
- Validate the frequency search method by conducting SPOD analysis on two interacting jets. Show that two coherent sources can create non-rank spectrums.
- Attempt additional methods of measuring the upstream structures, perhaps by tracing the waves instead of using SPOD.
- Attempt to understand the flowfield using computational methods. In particular, this may enable additional techniques such as Input-Output Analysis.
- Analyze the interaction of the upstream acoustic waves at the separation point.

REFERENCES

Awasthi, M., McCreton, S., Moreau, D. J., & Doolan, C. J. (2022). Supersonic cylinder wake dynamics. Journal of Fluid Mechanics, 945, A4.

Gowen, F. E., & Perkins, E. W. (1953). Drag of circular cylinders for a wide range of Reynolds numbers and Mach numbers (NACA TN 2960). National Advisory Committee for Aeronautics.

King, R. (1977). A review of vortex shedding research and its application. Ocean Engineering, 4(3), 141–171. https://doi.org/10.1016/0029-8018(77)90002-6

National Aeronautics and Space Administration. (1960). Project Mercury - A Chronology. Part 2 (A).

Price, T. J., Gragston, M., & Kreth, P. A. (2020). Modal Analysis of a Mach 1.5 Underexpanded Jet using Time-Resolved Optical Diagnostics. AIAA SciTech 2020 Forum.

Schmidt, B. E., & Shepherd, J. E. (2015). Oscillations in cylinder wakes at Mach 4. Journal of Fluid Mechanics, 785, R3. https://doi.org/10.1017/jfm.2015.668

Schmidt, O. T., & Colonius, T. (2020). Guide to Spectral Proper Orthogonal Decomposition. AIAA Journal, 58(3), 1023-1033.

Settles, G. S. (2001). Schlieren and Shadowgraph Techniques (1st ed.). Springer Berlin Heidelberg.

Thasu, P. S., & Duvvuri, S. (2022). Strouhal number universality in high-speed cylinder wake flows. arXiv preprint arXiv:2206.02645v1.

Venkatakrishnan, L., & Meier, G. (2004). Density Measurements Using the Background Oriented Schlieren Technique. Experiments in Fluids. 37. 10.1007/s00348-004-0807-1.

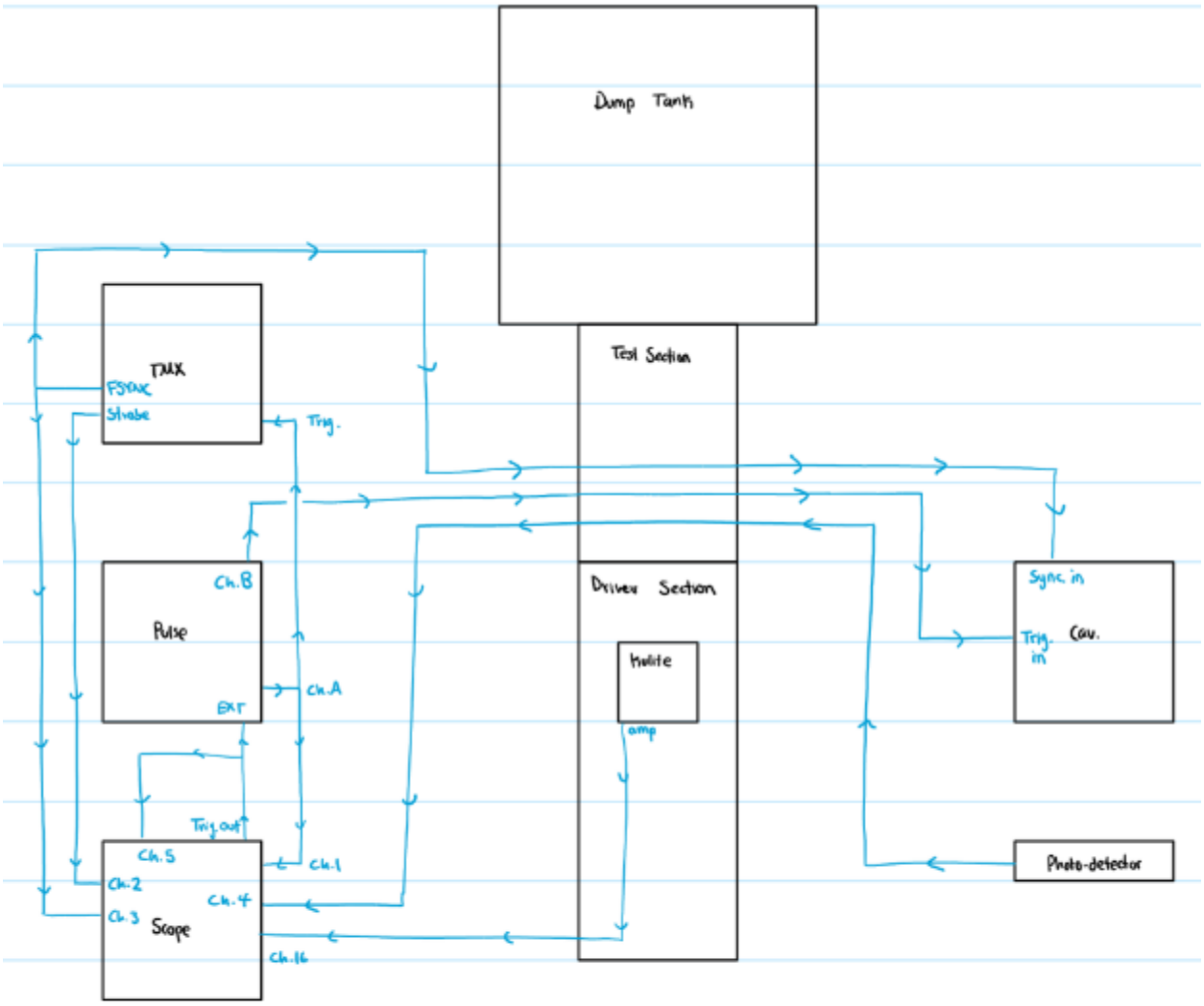
White, F. (1994). Fluid Mechanics (3rd ed.). McGraw-Hill.

APPENDIX

SHOT LOG

Shot Number	$\boldsymbol{D}$ **(mm)**	$\boldsymbol{P_0}$ **(kPa)**	$\boldsymbol{Re_D}$	**Schlieren Notes**
TL1	19	250		
TL2	19	250		
TL3	19	250		
TL4	19	250		
TL5	19	250		
TL6	19	250		
TL7	19	250		
TL8	19	250		
TL9	19	227	$1.96E5$	PI2000, horizontal
TL10	19	227	$1.96E5$	PI1000, horizontal
TL11	19	227	$1.96E5$	PI3200, horizontal, ND down to PI1600
TL12	19	227	$1.96E5$	No cutoff
TL13	19	319	$2.76E5$	PI3200, horizontal, ND down to PI 1600
TL14	19	183	$1.58E5$	PI3200, horizontal, ND down to PI 1600
TL15	19	136	$1.18E5$	PI3200, horizontal, ND down to PI 1600
TL16	19	103	$8.90E4$	PI3200, horizontal, ND down to PI 1600 (scope fail)
TL17	19	103	$8.90E4$	PI3200, horizontal, ND down to PI 1600
TL18	19	227	$1.96E5$	PI3200, true horizontal, ND down to PI 1600
TL19	19	227	$1.96E5$	PI1000, vertical
TL20	19	132	$2.67E5$	PI2500, horizontal, ND down to PI 1400
TL21	44.5	132	$2.67E5$	PI2500, horizontal, ND down to PI 1400
TL22	44.5	242	$4.89E5$	PI2500, horizontal, ND down to PI 1400

LUDWIEG SCHLIEREN WIRING DIAGRAM



CAMERA TRIGGERING NOTES

High speed Recording settings (200,000 fps)

Cavilux Settings:

Speed : high

Sync Polarity : falling

Sync Delay : 0 us

Pulse Patterns :

	cam 1	Laser 1
0	0.00 us	1.00 us
1	2.00 us	0.03 us

TMX Settings:

Sample Rate : 200,000

Exposure time : 2 us

Cam signal → strobe → width : 2.00 us

Scope Settings:

Single trigger, rising, 0.08V (80mV)

Live view/Focusing setting

Cavilux Settings:

Speed : normal

Pulse settings : continuous

Sync Polarity : falling

Sync Delay : 0 us

Pulse Patterns :

	cam 1	Laser 1
0	0.00 us	2.50 us
1	5.00 us	0.03 us

TMX Settings:

Sample Rate : 1000 fps

Exposure time : 5 us

Cam signal → strobe → width : 5.00 us

Scope Settings:

normal trigger, falling, 2.50V, channel 2 (strobe)

Sequence of Events

1. Camera is armed, Laser is armed, Scope is set on Run/Stop (*awaiting trigger*), and Pulse Generator awaits external trigger signal.
2. Startup shock passes through the nozzle Kulite transducer, creating a jump in voltage from raised pressure.
3. Scope reads startup voltage increase and triggers off of the rising edge.
4. Scope sends out a trigger signal to the Pulse Generator, which is simultaneously read into Scope Ch. 5.
5. Pulse Generator triggers from external triggering, and sends a trigger signal to the TMX trig. in and Cavilux trig. in.